Controlling and Characterizing Quantum Material Dynamics via Nonlinear Terahertz Spectroscopy

Thesis by
Pin-Hsun Hsieh

In Partial Fulfillment of the Requirements for the
degree of
Doctor of Philosophy

CALIFORNIA INSTITUTE OF TECHNOLOGY
Pasadena, California

2027
Defended June 4th, 2026

Pin-Hsun Hsieh
ORCID: 0000-0003-3854-9034

ACKNOWLEDGEMENTS

I would like to express my deepest appreciation to my graduate student mentor, Haw-Wei Lin. You have been a profoundly important figure throughout my graduate school journey. From the moment I joined the Blake group during the COVID, when you provided incredible live lab shadowing over Zoom, to teaching me how to craft a compelling scientific proposal, your guidance has been invaluable. Together, we built a single-shot TDS on an oscillator, and you taught me how to navigate the complexities of the 2D-terahertz-terahertz Raman spectrometer. Your expertise in data interpretation is unmatched. Whenever I had questions, you consistently provided insightful advice on how to design and interpret complex datasets, even after your graduation from the group. I have always valued our discussions, and I continue to learn an immense amount from your knowledge, insight, and feedback.

I also want to thank my advisor, Geoff Blake. Thank you for giving me the chance to join your group and for granting me the tremendous freedom to explore the science I am passionate about. Without your support, I would not have been able to discover so much fascinating science during my PhD. Thank you for giving me the space to grow from someone with no experience in instrument building into a scientist capable of constructing complex setups and capturing compelling data across a variety of materials.

I would also like to thank my committee members, Mitchio Okumura, Scott Cushing, and Kim See, for their invaluable feedback on my proposals and for their guidance on how to become a better scientist conducting rigorous research.

Thank you to all the members of the Blake group: Haw-Wei, Kyle, Jax, Sadie, Olivia, Cam, Alex, Tomislav, Maria, Evan, Evie, Aaron, and Victor. It has been a great pleasure working alongside you. I am deeply grateful for your help in navigating the challenges of experiments, candidacy, and the job search, as well as for your continuous encouragement during the more difficult moments of my PhD. Furthermore, I must extend my gratitude to my collaborator, Satoshi. Thank you for bringing our collaboration to life and for traveling all the way from Japan to California to work together. The materials you provided and the challenging scientific problems behind them are highly impactful and truly worth studying. It has been an honor to work with you.

Finally, and most importantly, I want to thank my wife, Yu-Ling. I will never forget

the moment you received your admission to Caltech. Studying abroad 7,000 miles away from home for six years would have been impossible without you. Thank you for being by my side for the past eleven years and for supporting my success in earning this degree. I would also like to thank my Dad, Mom, and brother for their endless support and for encouraging me to pursue my dream here in the United States.

ABSTRACT

This dissertation explores the development and application of advanced terahertz spectroscopy with nonlinear optical techniques to characterize and manipulate quantum materials and complex structural dynamics. First, a sensitive imaging method is presented for characterizing nonlinear terahertz beam profiles. This technique optimizes $\chi^{(3)}$ light-matter interactions and facilitates the realization of two-dimensional terahertz spectroscopy using multiple emitters. Such advancements enable the direct observation of fast picosecond dynamics in liquids and solids that remain difficult to probe in single-emitter configurations. Second, the research investigates the driver of the phase transition in the candidate excitonic insulator Ta_2NiSe_5. A novel geometric gating technique is introduced to disentangle structural and electronic orders using intense sub-picosecond terahertz pulses. By intentionally misaligning the incident electric field from the highly anisotropic tunneling trajectory, adiabatic carrier generation is suppressed. This transitions the system into a direct Impulsive Stimulated Raman Scattering regime and allows for the coherent pumping of the structural shear mode while preserving the many-body excitonic condensate. Driving this macroscopic lattice deformation without destroying the electronic condensate proves that the spontaneous structural distortion origins from an intrinsic lattice instability, establishing a robust framework for the optical control of quantum materials. Finally, the thesis addresses the necessity of dynamic terahertz polarization control for breaking time-reversal symmetry in Floquet engineering. Through multidimensional Terahertz-Terahertz-Raman spectroscopy, the ultrafast nonlinear optical response of (110)-cut cubic zinc sulfide is analyzed. The study attributes anomalous low-frequency spectral oscillations to a macroscopic phase mismatch between the co-propagating terahertz pump and optical probe. Exploiting this temporal walk-off gives the direct extraction of a highly anisotropic transient refractive index. By tuning the crystallographic azimuthal angle, the terahertz-induced birefringence satisfies the conditions for a broadband zero-order terahertz quarter-waveplate. Relying on a transient nonlinear response rather than physical thickness, this proposed platform provides a powerful pathway for generating circularly polarized terahertz pulses for the on-demand optical manipulation of quantum materials.

PUBLISHED CONTENT AND CONTRIBUTIONS

[1] Haw-Wei Lin et al. “Characterization of the nonlinear THz focus for 2D THz spectroscopy”. *Journal of the Optical Society of America B* 41.2 (2024), p. 466.
H.W. Lin and P.H. Hsieh developed the technique and performed the experiments. H.W. Lin prepared the manuscript with input from P.H. Hsieh, G.Mead, and G.A. Blake.

TABLE OF CONTENTS

LIST OF ILLUSTRATIONS

Number *Page*

[Part of the LIST OF ILLUSTRATIONS is temporarily embargoed.]

Chapter 1

INTRODUCTION

Understanding and controlling the macroscopic quantum ground states of complex materials represents a central frontier in modern condensed matter physics [1, 2]. In recent years, advancements in the generation of ultrafast broadband terahertz pulses (0.1 to 10 THz, 3.3 to 333 cm^{-1}, λ = 3000 to 30 μm) have unlocked previously inaccessible pathways for exploring these phenomena. By providing peak electric fields exceeding 0.1 MV/cm and broad bandwidths, intense terahertz pulses enable the direct, coherent manipulation of low-energy collective excitations such as phonons [3, 4], Cooper pairs [5, 6], and magnons [7]. This dissertation is motivated by the critical need to advance nonlinear terahertz methodologies to characterize and dynamically control the fundamental properties of quantum materials on macroscopic scales.

A primary requirement for pushing the boundaries of nonlinear spectroscopy is the precise spatiotemporal control of the driving electromagnetic fields. Ultrafast two-dimensional terahertz spectroscopy has emerged as a powerful technique to deconvolve complex dynamics and coupling information [8–10]. However, investigating sub-picosecond nuclear dynamics in solids and liquids requires a two-emitter geometry to bypass the nonlinear interactions that plague single-emitter configurations [11–13]. This multi-pulse arrangement presents severe alignment challenges. Furthermore, conventional imaging tools lack the sensitivity and appropriate response mechanisms to isolate the precise focal region where higher-order light-matter interactions occur [14–17]. To address this, the first major focus of this dissertation establishes a highly sensitive imaging technique utilizing the $\chi^{(3)}$ response of gallium phosphide. By effectively isolating the nonlinear interaction area, this methodology provides the critical spatial characterization necessary to optimize multi-pulse terahertz experiments, laying a robust technical foundation for advanced material investigations.

Building upon this sophisticated spectroscopic framework, the research subsequently addresses the drivers of spontaneous phase transitions. The candidate excitonic insulator Ta_2NiSe_5 provides a suitable platform for such studies, as it features a macroscopic quantum ground state driven by electron-hole condensation [18, 19].

A pervasive roadblock in studying this material is the inextricable entanglement of its electronic phase transition with an orthorhombic to monoclinic structural lattice shear [20, 21]. Conventional above-bandgap excitation inevitably melts the condensate, triggering a complex picosecond electronic relaxation process that obscures the causal sequence of the transition [22, 23]. To bypass this limitation, we introduce a novel geometric gating technique utilizing intense sub-bandgap terahertz pulses. By precisely misaligning the driving field from the highly anisotropic Ta-Ni interband tunneling trajectory, we successfully suppress free carrier generation and selectively excite the structural shear mode. Isolating this purely structural perturbation provides a definitive experimental framework to test the origin of the excitonic insulator transition.

Finally, the dissertation extends the application of tailored terahertz fields to the transient engineering of topological states. Floquet engineering utilizes time-periodic optical electromagnetic driving fields to restructure the electronic energy landscape, offering on-demand control over exotic phases of matter [24–27]. Dynamically breaking time-reversal symmetry to open a topological mass gap explicitly requires circularly polarized light. While successful in the near-infrared regime, selectively targeting the foundational excitations of solids requires translating these tailored driving fields into the terahertz domain. Overcoming the severe bandwidth limitations of conventional static optics is essential for this goal [28, 29]. By exploiting transient nonlinear responses and dynamic polarization control, this work proposes a prototype platform to develop the necessary tools to generate broadband circularly polarized terahertz pulses. Together, these methodologies demonstrate how refining the fundamental capabilities of nonlinear terahertz spectroscopy unlocks new paradigms for characterizing and engineering the dynamic properties of quantum materials.

References

[1] L. V. Keldysh and Yu. V. Kopaev. “Possible instability of the semimetallic state toward Coulomb interaction”. *Soviet Physics Solid State* 6 (1965), pp. 2219–2224.

[2] Jacques Des Cloizeaux. “Exciton instability and crystallographic anomalies in semiconductors”. *Journal of Physics and Chemistry of Solids* 26.2 (1965), pp. 259–266.

[3] Haw-Wei Lin, Griffin Mead, and Geoffrey A. Blake. “Mapping LiNbO 3 Phonon-Polariton Nonlinearities with 2D THz-THz-Raman Spectroscopy”. *Physical Review Letters* 129.20 (2022), p. 207401.

[4] M. Kozina et al. “Terahertz-driven phonon upconversion in SrTiO3”. *Nat. Phys.* 15.4 (2019), pp. 387–392.

[5] D. Fausti et al. “Light-Induced Superconductivity in a Stripe-Ordered Cuprate”. *Science* 331.6014 (2011), pp. 189–191.

[6] W. Hu et al. “Optically enhanced coherent transport in YBa2Cu3O6.5 by ultrafast redistribution of interlayer coupling”. *Nature Mater* 13.7 (2014), pp. 705–711.

[7] Lin Huang et al. “Terahertz oscillation driven by optical spin-orbit torque”. *Nat Commun* 15.1 (2024), p. 7227.

[8] Thomas Elsaesser, Klaus Reimann, and Michael Woerner. “Focus: Phase-resolved nonlinear terahertz spectroscopy - From charge dynamics in solids to molecular excitations in liquids”. *Journal of Chemical Physics* 142.21 (2015).

[9] Harold Y. Hwang et al. “A review of non-linear terahertz spectroscopy with ultrashort tabletop-laser pulses”. *Journal of Modern Optics* 62.18 (2015), pp. 1447–1479.

[10] Peter Hamm et al. “Perspective: THz-driven nuclear dynamics from solids to molecules”. *Structural Dynamics* 4.6 (2017).

[11] Frank Y. Gao et al. “High-speed two-dimensional terahertz spectroscopy with echelon-based shot-to-shot balanced detection”. *Optics Letters* 47.14 (2022), p. 3479.

[12] Griffin Mead et al. “Sum-Frequency Signals in 2D-Terahertz-Terahertz-Raman Spectroscopy”. *Journal of Physical Chemistry B* 124.40 (2020), pp. 8904–8908.

[13] Haw-Wei Lin, Griffin Mead, and Geoffrey A. Blake. “ Mapping LiNbO 3 Phonon-Polariton Nonlinearities with 2D THz-THz-Raman Spectroscopy ”. *Physical Review Letters* 129.20 (2022), p. 207401.

[14] Hichem Guerboukha, Kathirvel Nallappan, and Maksim Skorobogatiy. “Toward real-time terahertz imaging”. *Advances in Optics and Photonics* 10.4 (2018), p. 843.

[15] Mostafa Shalaby, Carlo Vicario, and Christoph P. Hauri. “High-performing nonlinear visualization of terahertz radiation on a silicon charge-coupled device”. *Nature Communications* 6 (2015), pp. 1–5.

[16] O. V. Chefonov et al. “Terahertz beam spot size measurements by a CCD camera”. *Optics Letters* 44.17 (2019), p. 4099.

[17] Q. Wu, T. D. Hewitt, and X.-C. Zhang. “Two-dimensional electro-optic imaging of THz beams”. *Applied Physics Letters* 69.8 (1996), pp. 1026–1028.

[18] C. Comte and P. Nozières. “Exciton Bose condensation : the ground state of an electron-hole gas - I. Mean field description of a simplified model”. *Journal de Physique* 43.7 (1982), pp. 1069–1081.

[19] Edoardo Baldini et al. “The spontaneous symmetry breaking in Ta_2 $NiSe_5$ is structural in nature”. *Proc. Natl. Acad. Sci. U.S.A.* 120.17 (2023), e2221688120.

[20] H. Ning et al. “Signatures of Ultrafast Reversal of Excitonic Order in Ta 2 NiSe 5”. *Phys. Rev. Lett.* 125.26 (2020), p. 267602.

[21] Selene Mor et al. “Ultrafast Electronic Band Gap Control in an Excitonic Insulator”. *Phys. Rev. Lett.* 119.8 (2017), p. 086401.

[22] Takeshi Suzuki et al. “Detecting electron-phonon coupling during photoinduced phase transition”. *Phys. Rev. B* 103.12 (2021), p. L121105.

[23] Kozo Okazaki et al. “Photo-induced semimetallic states realised in electron–hole coupled insulators”. *Nat Commun* 9.1 (2018), p. 4322.

[24] Changhua Bao et al. “Light-induced emergent phenomena in 2D materials and topological materials”. *Nat Rev Phys* 4.1 (2021), pp. 33–48.

[25] Y. H. Wang et al. “Observation of Floquet-Bloch States on the Surface of a Topological Insulator”. *Science* 342.6157 (2013), pp. 453–457.

[26] Marco Merboldt et al. “Observation of Floquet states in graphene”. *Nat. Phys.* 21.7 (2025), pp. 1093–1099.

[27] Michael Schüler et al. “How Circular Dichroism in Time- and Angle-Resolved Photoemission Can Be Used to Spectroscopically Detect Transient Topological States in Graphene”. *Phys. Rev. X* 10.4 (2020), p. 041013.

[28] Daniel G. Suárez-Forero et al. “Chiral flat-band optical cavity with atomically thin mirrors”. *Sci. Adv.* 10.51 (2024), eadr5904.

[29] Johan Andberger et al. “Terahertz chiral subwavelength cavities breaking time-reversal symmetry via ultrastrong light-matter interaction”. *Phys. Rev. B* 109.16 (2024), p. L161302.

Chapter 2

CHARACTERIZATION OF THE NONLINEAR THZ FOCUS FOR 2D THZ SPECTROSCOPY

Adapted with permission from:
Haw-Wei Lin, **Pin-Hsun Hsieh**, Griffin Mead, and Geoffrey A. Blake*, "Characterization of the nonlinear THz focus for 2D THz spectroscopy," J. Opt. Soc. Am. B 41, 466-470 (2024)

2.1 Abstract

We present a sensitive imaging method capable of the selective characterization of the nonlinear THz beam profile, providing a direct handle to optimize $\chi^{(3)}$ light-matter interactions that are critical to two-dimensional (2D) THz spectroscopies. In particular, this method facilitates the development of experimentally-challenging 2D THz spectroscopies with multiple THz emitters, which enables direct investigations of fast picosecond dynamics in liquids and solids that are challenging in single-emitter 2D THz spectroscopic setups.

2.2 Introduction

In recent years, advancements in the generation of ultrafast broadband terahertz (THz) pulses, reaching above 1 MV/cm in peak electric field strengths and exceeding 10 THz in bandwidth, have enabled novel investigations of various condensed matter phenomenon using nonlinear THz spectroscopy [1, 2]. In particular, ultrafast two-dimensional (2D) THz spectroscopic techniques have attracted significant attention due to their unique capability to deconvolve and extract dynamics and coupling information from broad THz spectral features [3]. Recent demonstration of various types of 2D THz spectroscopies have provided detailed characterization of the fast reorientation dynamics (100s of fs) of water and aqueous solutions [4, 5], measured nonlinear rotational echos (100s of ps) in the gas phase [6], and directly observed nonlinear coupling interactions of phonon-polariton (5-10 ps) [7] as well as magnon (10s of ps) modes [8].

A number of the available 2D THz techniques, including 2D THz spectroscopy [6, 8, 9] and 2D THz-THz-Raman (2D-TTR) spectroscopy [7, 10], employ multiple THz pump pulses that must be temporally and spatially overlapped at

the sample. Researchers have developed two primary experimental layouts for 2D THz spectroscopy to achieve this. In the single-emitter geometry, two time-delayed optical or mid-infrared (mid-IR) pump beams are combined co-linearly prior to the THz emitter crystal to generate two co-linear THz emission pulses, which are focused with off-axis parabolic (OAP) mirrors to achieve sufficiently high THz peak field strengths [6, 8, 9, 11]. While this method provides ease of alignment, time-delays within a few ps cannot be easily accessed due to nonlinear interactions between pump pulses in the THz emitter crystal [6], making investigation of room-temperature vibrational dynamics (typically < 10 ps in lifetime) in liquids and solids challenging.

To access fast nuclear dynamics, one can instead combine two THz pulses from two individual THz emitters to eliminate interactions in the emitter crystal. 2D-TTR spectroscopy with this two-emitter geometry has successfully demonstrated investigation of ps-vibrational dynamics in organic halogenated liquids [10] and nonlinear couplings of phonon-polaritons in $LiNbO_3$ [7]. Typically, a wire-grid polarizer (WGP) is used to combine two orthogonally polarized THz beams co-linearly into the OAP relay due to the lack of THz-compatible beam splitters. The tight-focusing OAP relay can introduce significant aberrations to the THz mode quality and the spatial overlap of the multiple THz pulses if not properly aligned, leading to significant decrease in signal-to-noise. Thus, characterization of the spatial, temporal, and field strength parameters of the co-linear THz pump pulses at the sample position is crucial to ensure consistent and reliable measurements with 2D THz spectroscopy. For the temporal and field strength information of the THz pulses, there are several well-established methods such as electro-optic (EO) sampling [12, 13] and air-breakdown coherent detection (ABCD) [14]. However, imaging tools available for visualizing the spatial distribution of intense THz pulses at the focal region are significantly more limited [15]. Off-the-shelf THz camera products often employ bolometer- or pyroelectric-based detectors [16], which have large pixel sizes (typically $> 15\mu$m), slow response times, and long read-out times [17]. The use of additional filters and attenuators are generally necessary to block ambient thermal background and prevent saturation, which can disperse and distort the spatial profile of the THz focus. More recently, Si-based charge-coupled device (CCD) cameras have been shown to be able to directly detect THz photons through an electron tunneling mechanism [17, 18]. However, due to the large mismatch in THz photon energy (few meV) and the bandgap of Si ($\sim$1.1 eV), the sensitivity is moderate with a detection limit around 5 MV/cm in THz field strength [18].

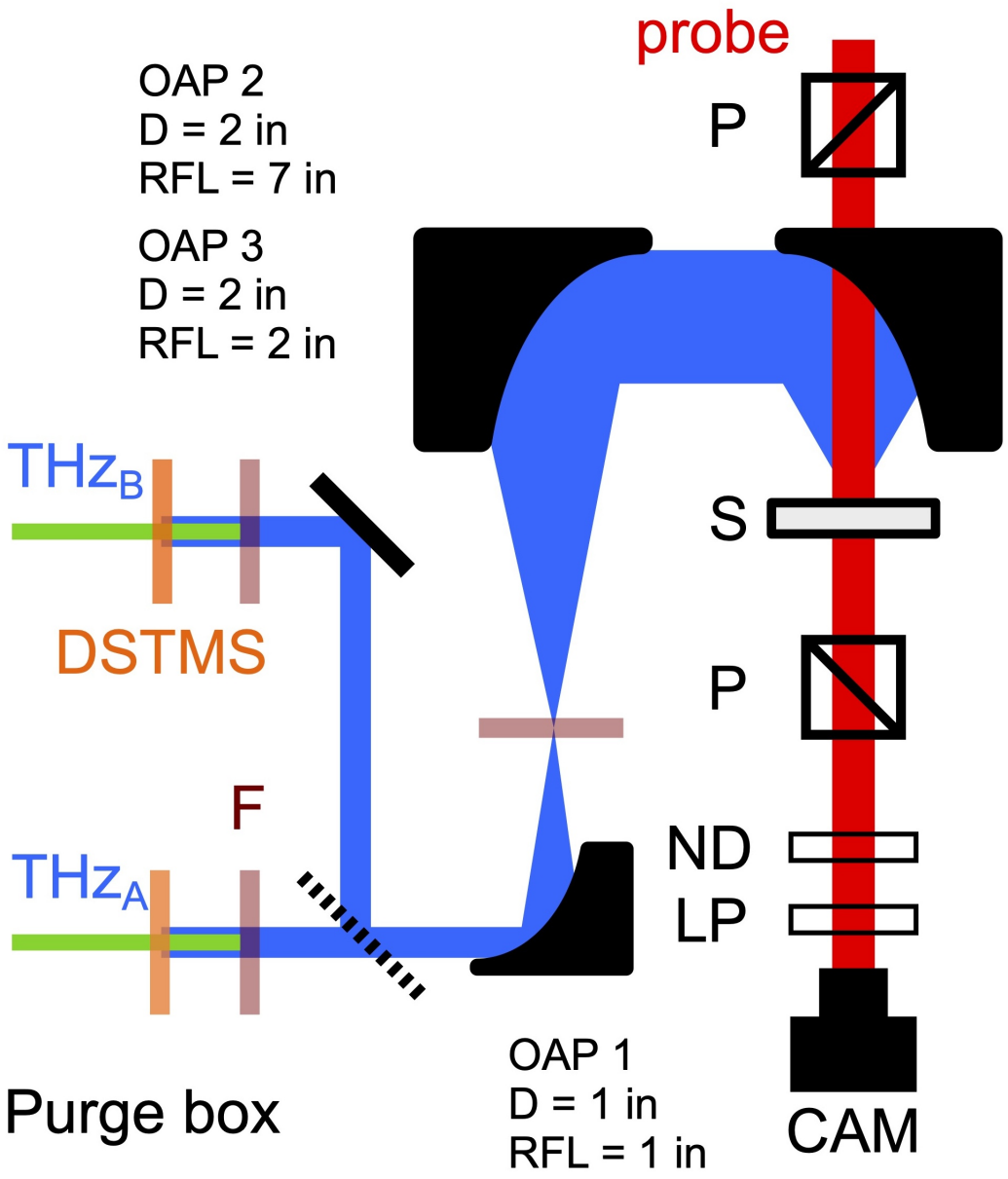

Figure 2.1: Experimental layout for the nonlinear imaging technique. F: 20 THz long-pass filter (QMC Instruments); P: polarizers; WGP: wire-grid polarizer; S: sample/100 μm GaP; ND: neutral density filter; LP: 750 nm long-pass filter; L: imaging lens. Green: 1.4 μm pump pulse; Red: 800 nm probe; Blue: THz pump pulse.

2D-EO imaging techniques, initially developed by Wu et. al.[19], utilizes the $\chi^{(2)}$ response of EO crystals to measure THz electric field distributions. However, as the $\chi^{(2)}$ response is linear in THz field strength, 2D-EO imaging does not provide adequate characterization of the nonlinear focus where $\chi^{(3)}$ light-matter interactions

measured by 2D THz spectroscopy take place. Thus, there is need for a sensitive imaging method to selectively characterize the nonlinear beam profile of two-emitter 2D THz spectroscopies to allow rigorous signal optimization.

In this work, we utilize the $\chi^{(3)}$ response of GaP to provide spatial characterization of the nonlinear THz focus. Using differential chopping and a fast frame-rate camera, the $\chi^{(3)}$ interaction area of 2D THz spectroscopy was selectively isolated from other lower order signals. We demonstrate the ease of implementation of this novel imaging method in 2D-TTR spectroscopy, where modifications were made only to the probe beam path. This technique will facilitate the development of 2D THz spectroscopies in the study of important fast vibrational dynamics in liquids and solids.

2.3 Experimental Setup

An experimental schematic of the nonlinear imaging technique applied to 2D-TTR spectroscopy is shown in **Fig. 2.1**. Two broadband THz pump pulses (1-8 THz) are generated from two DSTMS [20] emitter crystals (Swiss THz) with the 1.4 μm output of an optical parametric amplifier (OPA), each 250 μJ per pulse. The THz pulses are orthogonally-polarized and combined with a wire-grid polarizer to be co-linear before entering a three-OAP relay, which expands and tightly focuses the THz pulses at the sample position. Crucially, the imaging technique makes no insertion or modification to the THz beam paths. As a result, optimized THz pulses can be directly incorporated into 2D-TTR spectroscopy with only changes to probe detection optics. A 100 μm thick, <110> oriented GaP crystal is placed precisely at the focus of the last OAP with a computer-controlled stepper-motor stage. A near-IR probe pulse (800 nm, 35 fs) illuminates an area of the crystal larger than that of the THz focus. We adapted the cross-polarized detection scheme in 2D-EO imaging [19], which provides extremely low background and greater than 10^8 extinction ratios. This sensitive detection scheme is critical to the detection of the 2D optical intensity of rotated probe photons due to nonlinear interactions between the probe and THz pulses. A biconvex lens (f = 200 mm) is used to image the surface of the GaP crystal onto a fast frame rate sCMOS camera (ANDOR Zyla 5.5MP) with a 1:1 magnification. A 750 nm long-pass filter and a 2.00 ND filter are placed in front of the sCMOS camera to remove background contributions and avoid saturation. The filters are placed after the GaP crystal to avoid distortion of the THz beam. The typical EO sampled THz pulse shape and bandwidth in air is shown in **Fig. 2.2a** and **Fig. 2.2b** respectively. The oscillatory features after the main THz pulse are due to

water vapor.

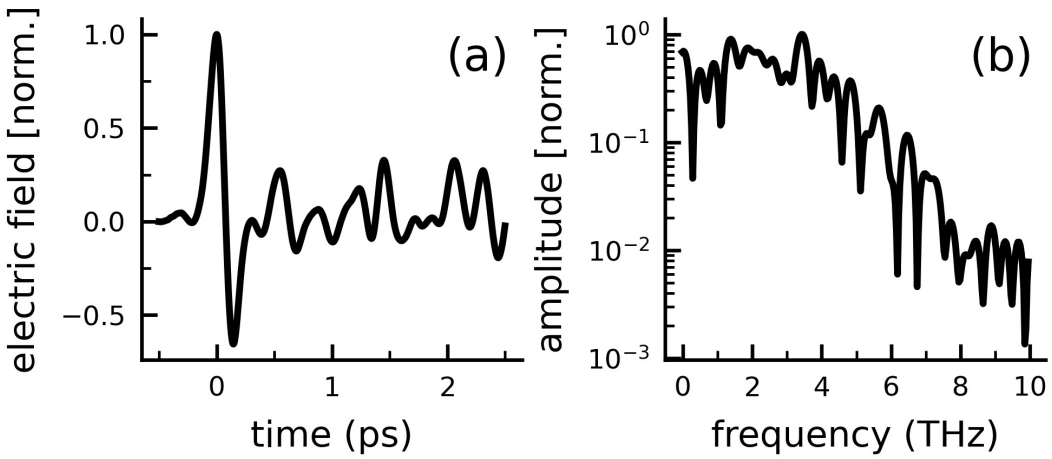

Figure 2.2: (a) Time-resolved, EO sampled THz_A pulse shape in air. (b) Corresponding bandwidth of THz_A obtained from Fourier Transform.

2.4 Results and Discussion

The key to selective isolation of the nonlinear THz overlap region is the differential chopping scheme we employ. Specifically, the camera operates at the laser repetition rate (1 kHz) with a region of interest (ROI) set to 40-by-40 pixels and an exposure time of 880 μs. The two THz beams THz_A and THz_B are modulated at $\frac{1}{2}$ (500 Hz) and $\frac{1}{3}$ (333.33 Hz) of the laser repetition rate, respectively. Due to the cross-polarized detection scheme, the camera response is sensitive to anisotropic light-matter interactions. Given the MV/cm THz field strengths employed in 2D THz spectroscopies, we consider both second-order (EO effect) and third-order (Kerr effect) anisotropic contributions to the image S, which is given as [21]

$$S \propto \chi^{(2)}(E_A^{THz} + E_B^{THz}) + \chi^{(3)}(E_A^{THz} + E_B^{THz})^2 \tag{2.1}$$

where E_A^{THz} and E_B^{THz} are the field strengths of the THz pulses THz_A and THz_B, and $\chi^{(2)}$ and $\chi^{(3)}$ are the second- and third-order nonlinear susceptibility of GaP, respectively. Expanding Eq. 2.1 yields fives nonlinear terms, which are the second-order terms $\chi^{(2)}E_A^{THz}$ and $\chi^{(2)}E_B^{THz}$, and the third-order terms $\chi^{(3)}(E_A^{THz})^2$, $\chi^{(3)}(E_B^{THz})^2$, and $\chi^{(3)}(E_A^{THz}E_B^{THz})$. The third-order term $\chi^{(3)}(E_A^{THz}E_B^{THz})$ in particular is proportional to the electronic component in a 2D-TTR spectra, which is given as

$$S_{TTR}^{el} \propto \chi^{(3)} I_{probe} E_A^{THz} E_B^{THz} \tag{2.2}$$

where I_{probe} is the probe intensity. Specifically, the electronic component provides a quantitative estimate of the signal strength of 2D-TTR spectroscopy [7, 10]. As a

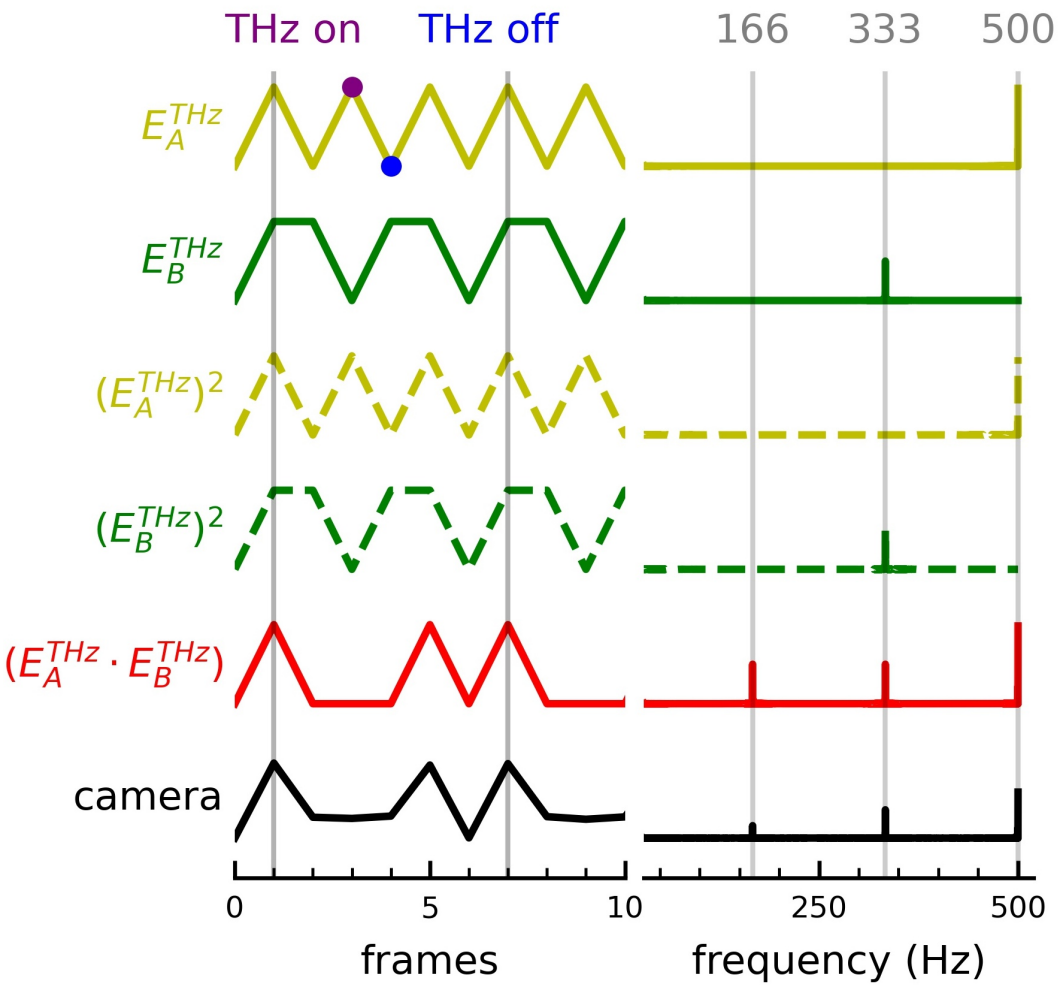

Figure 2.3: The differential chopping scheme. (Left) Time series of each individual nonlinear contribution to the camera response as a function of time. THz-on (purple) and THz-off (blue) frames are represented by 1 and 0 values. The camera trace shows the normalized amplitude of the center pixel in first 10 frames of a typical experimental measurement. (Right) Corresponding Fourier transform of each time series. The modulation frequencies (333 and 500 Hz) and the difference frequency (166 Hz) are highlighted.

result, imaging the intensity distribution of $\chi^{(3)} E_A^{THz} E_B^{THz}$, denoted as the nonlinear beam profile herein, on the surface of GaP provides a direct handle to optimize and improve the reliability of 2D-TTR experiments.

Fig. 2.3 shows the modulation of the five nonlinear terms as a function of time, where a THz-on and a THz-off frame are represented by 1 and 0 values, respectively (the magnitude of the nonlinear susceptibility tensors are omitted for clarity). The time traces for E_A^{THz} and E_B^{THz} are constructed according to their experimental modulation frequencies, while that for $(E_A^{THz})^2$, $(E_B^{THz})^2$, and $(E_A^{THz} E_B^{THz})$ are obtained from

simple multiplications of the E_A^{THz} and E_B^{THz} traces. We note that the phase of the optical chopper for THz$_B$ is chosen to result in an on-on-off time sequence that minimizes the number of laser shots blocked, as shown for the E_B^{THz} and $(E_B^{THz})^2$ traces. The Fourier transform of each time trace is shown at right, where clear peaks are observed at the modulation frequencies of E_A^{THz} (500 Hz), E_B^{THz} (333.33 Hz), and the difference frequency (166.66 Hz). In particular, the nonlinear term $\chi^{(3)}(E_A^{THz}E_B^{THz})$, which is precisely the signals of interest in 2D THz spectroscopy, is the only signal present at 166.66 Hz.

The experimentally measured camera signal is the sum of the five individual nonlinear contributions, which is shown in **Fig. 2.3** with the black curve. To isolate the distinct nonlinear contributions of the image, we perform a phase-sensitive frequency demodulation routine that is analogous to that of a lock-in amplifier, which measures the amplitude of the underlying signals at a certain frequency. Specifically, a sine-wave (reference signal) with the desired modulation frequency f (166.66, 333.33, or 500 Hz) is generated and multiplied with the camera time series, which frequency shifts each peak in the Fourier spectrum by f. Then, we compute the fast Fourier transform of the multiplication product and measure the amplitude at zero frequency (DC), which is also the amplitude at f in the camera series. The phase of the reference signal is chosen to maximize the amplitude of the demodulated DC peak.

The nonlinear terms that contribute to each modulation frequency are evident from the Fourier transform spectra shown in **Fig. 2.3**. Applying the demodulation procedure, we decompose the camera signal into three distinct channels: S_{500} at 500 Hz, which includes the $\chi^{(2)}E_A^{THz}$, $\chi^{(3)}(E_A^{THz})^2$, and $\chi^{(3)}E_A^{THz}E_B^{THz}$ contributions; S_{333} at 333.33 Hz, which includes the $\chi^{(2)}E_B^{THz}$, $\chi^{(3)}(E_B^{THz})^2$, and $\chi^{(3)}E_A^{THz}E_B^{THz}$ contributions; and S_{166} at 166.66 Hz, which contains only the nonlinear term $\chi^{(3)}E_A^{THz}E_B^{THz}$. In particular, because the $\chi^{(3)}E_A^{THz}E_B^{THz}$ trace is not an ideal sine-wave, its contribution is not only present at the fundamental frequency of 166.66 Hz, but also its harmonics at 333.33 and 500 Hz. The ratios between the amplitudes at the harmonic frequencies (A_{333} and A_{500}) and the fundamental frequency (A_{166}) are uniquely dependent on the shape of the pulse train and can be determined by computing its Fourier transform, as shown in **Fig. 2.3**. For the $\chi^{(3)}E_A^{THz}E_B^{THz}$ trace in our work, $\frac{A_{333}}{A_{166}} = 1$ and $\frac{A_{500}}{A_{166}} = 2$. Thus, we can rearrange the demodulation

products to obtain three signals:

$$\begin{aligned} S_A &= (S_{500} - 2S_{166}) \propto \chi^{(2)} E_A^{THz} + \chi^{(3)} (E_A^{THz})^2 \\ S_B &= (S_{333} - S_{166}) \propto \chi^{(2)} E_B^{THz} + \chi^{(3)} (E_B^{THz})^2 \\ S_{A+B} &= S_{166} \propto \chi^{(3)} E_A^{THz} E_B^{THz} \end{aligned}$$

where contributions from the nonlinear third-order signal and that solely from E_A^{THz} and E_B^{THz} are separated. In particular, selective isolation of the nonlinear beam profile $\chi^{(3)} E_A^{THz} E_B^{THz}$ can be achieved by demodulation of the time series at $\frac{1}{6}$ of the laser repetition rate, which yields the S_{A+B} signal. This signal decomposition is verified later in this work through experiments with varying THz electric field strengths.

Fig. 2.4a shows the nonlinear beam profile, S_{A+B}, measured on 100 μm GaP obtained by applying the demodulation routine to each individual pixel of the ROI in a 10,000-shot (10 seconds) time series. Temporal overlap of the THz_A, THz_B, and probe beams were optimized with two optical delay stages, which controlled the path lengths of the THz_B and probe beams. The optical axis of the GaP crystal is set at 45° between the polarization of the two orthogonally-polarized THz pump beams to minimize second order contributions to S_A and S_B [22]. The nonlinear beam profile is fitted with a general two-dimensional elliptical Gaussian distribution, yielding $(1/e_x^2, 1/e_y^2)$ beam diameters of (147 μm, 187 μm). Recall that the intensity of the nonlinear beam profile is proportional to the nonlinear observable measured in 2D THz spectroscopies. Thus, the nonlinear imaging method enables rigorous optimization of the spatial and temporal overlap of the two THz pump beams to minimize spot size and maximize signal strength of 2D spectroscopy. Further, the high signal-to-noise nonlinear beam profile was obtained with a 10 second time series and few seconds of post-processing, allowing near real-time characterization during experimental alignment procedures. In addition, nonlinear imaging allows precise placement of samples with small physical dimensions within the nonlinear interaction area of the THz pump beams. This is particularly important for the analysis of novel quantum materials, whose synthesis often yield flakes few 100 μm in diameter, which is comparable to the THz interaction area in this work.

To verify the signal decomposition described above, we characterized the THz field strength dependence of the differentially modulate signals S_A, S_B, and S_{A+B}. 10,000-shot kinetic series were taken on 100 μm GaP with variable THz_A and

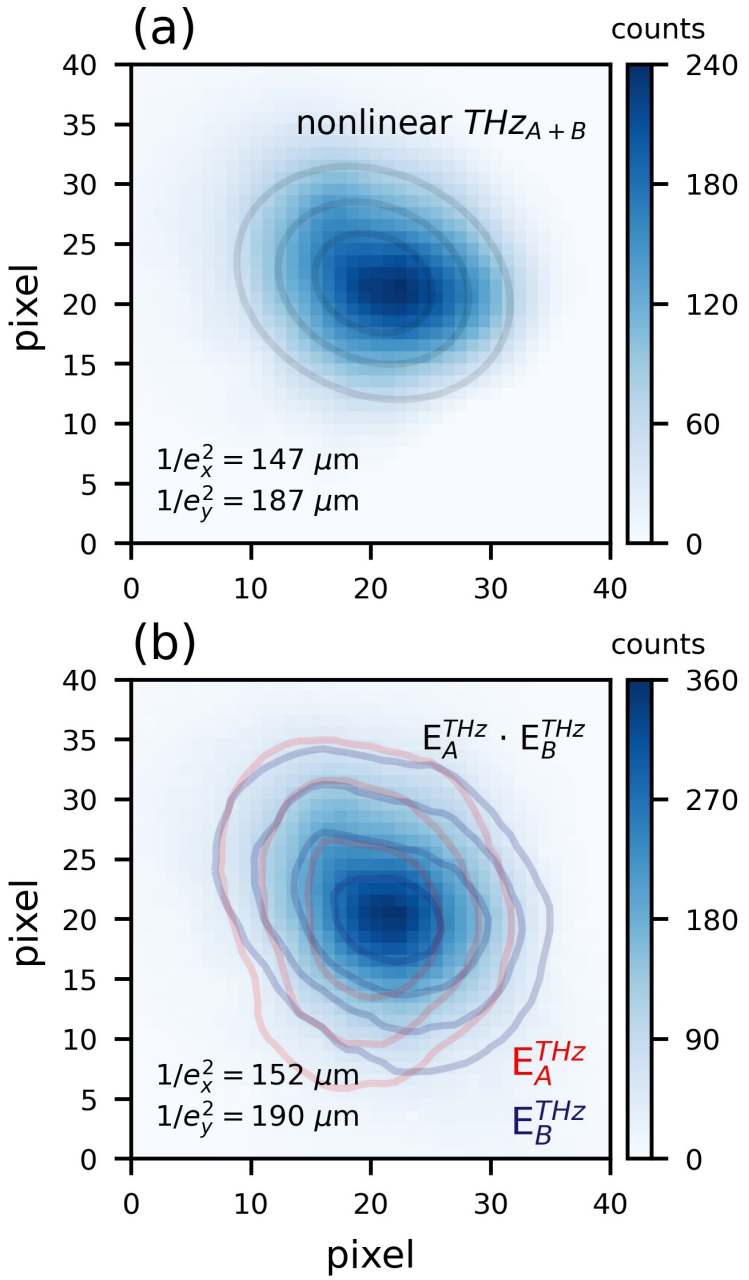

Figure 2.4: (a) Nonlinear beam profile of 2D-TTR spectroscopy. Grey contours show the best fit 2D Gaussian distribuion. (b) Simulated nonlinear beam profile from the product of experimentally measured E_A^{THz} (red contours) and E_B^{THz} (blue contours) distributions.

fixed THz_B field strengths. The kinetic series of images were processed with the demodulation procedure described previously (including the correction to the harmonic contributions of $\chi^{(3)} E_A^{THz} E_B^{THz}$) to obtain the images of S_A, S_B, and S_{A+B}. For clarity, the total intensity of the 40-by-40 pixel image is analyzed as a function

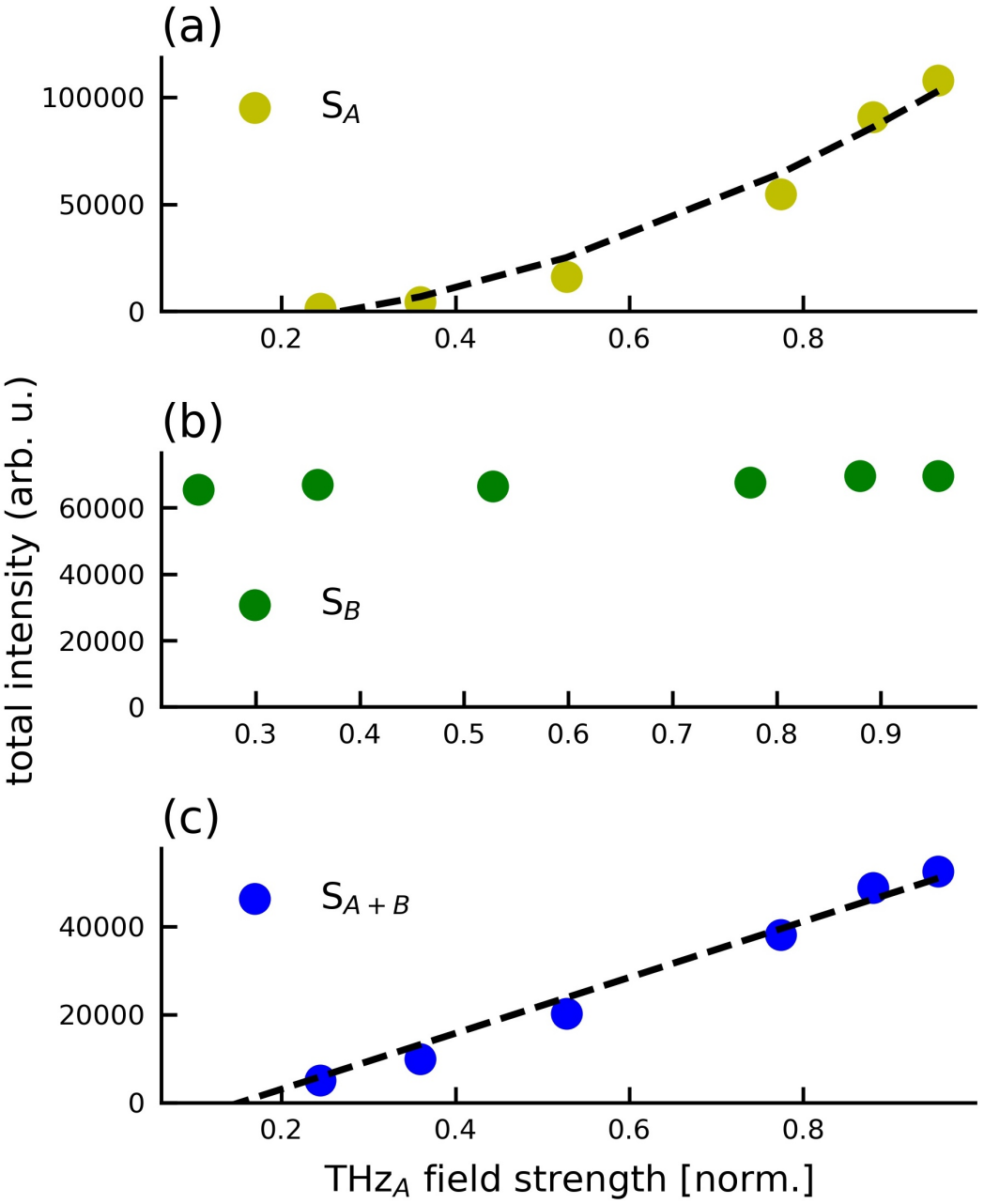

Figure 2.5: THz field strength dependence of the three differentially modulated channels (a) S_A, (b) S_B, and (c) S_{A+B}.

of THz_A field strength for each channel, as shown in **Fig. 2.5**. We note that the same trends are observed when the intensity of the beam center is used instead. The intensity of S_{A+B} (**Fig. 2.5c**) displays linear dependence with THz_A field strength, consistent with originating from the $\chi^{(3)} E_A^{THz} E_B^{THz}$ term. On the other hand, the intensity of S_B remains constant while that of S_A exhibits primarily a quadratic dependence with changing THz_A field strength, as shown in **Fig. 2.5a and b**. This

result is again consistent with our previous attribution of second- and third-order light matter interactions in S_A and S_B, which supports the demodulation and the harmonic amplitude correction routines. It further indicates that the third-order term $\chi^{(3)}(E^{THz})^2$ is dominant over the second-order term $\chi^{(2)}(E^{THz})$ at the THz field strengths of our experiments. Given the predominant third-order nature of the S_A and S_B signals, which is proportional to $\chi^{(3)}(E^{THz})^2$, a quantitative estimate of the beam profiles of E_A^{THz} and E_B^{THz} can be obtained from the square-root of the S_A and S_B images, respectively. As shown by the red and dark blue contours in **Fig. 2.4b**, the two THz beams are spatially well overlapped to within few μm (pixel size of 6.5 μm) with a $1/e^2$ radius of approximately 240 μm on average. The precise spatial overlap achieved between THz_A and THz_B pump beams, which were optimized utilizing the nonlinear imaging method presented in this work, highlights the consistency this method provides for 2D THz experiments. The nonlinear THz beam profile can further be estimated from multiplication of the E_A^{THz} and E_B^{THz} profiles, as shown with the blue filled contour in **Fig. 2.4b**. The beam parameters are determined with 2D elliptical Gaussian fitting to be $(1/e_x^2, 1/e_y^2)$ =(152 μm, 190 μm), which agrees well with the direct measurement of the nonlinear beam profile. Slight over-estimations ($\sim$ 3%) of the beam parameters are likely a result of the involvement of second-order effects in the S_A and S_B channels, which are difficult to separate from power-scaling experiments. When the field strength of E_A^{THz} is reduced to 35%, which increases the relative ratio of the second-order contributions, the over-estimations increase to $\sim$ 10%, supporting the above hypothesis. Note that the calculated nonlinear beam profile relies on the results of the THz field strength dependence experiments, which revealed the dominance of the third-order effect at the 100s kV/cm to MV/cm field strengths employed in 2D THz spectroscopies. Under these strong field conditions, 2D EO imaging techniques may significantly misrepresent the true THz beam profiles due to involvement of higher-order effects, if power dependence experiments were not performed. While THz attenuators can be used to reduce the impact of higher-order contributions, they also introduce undesirable spatial and frequency distortions of the THz beam.

2.5 Conclusion

To summarize, we have presented a sensitive imaging method for 2D THz spectroscopy that selectively characterizes the nonlinear beam profile $\chi^{(3)}E_A^{THz}E_B^{THz}$ through differential chopping. Implementation of the nonlinear imaging method is demonstrated on 2D-TTR spectroscopy, where identical THz pump beam paths

are retained and only minor modifications to the probe beam paths are made. This eliminates distortions to spatial and frequency distributions of the THz beams caused by attenuators that are often required by off-the-shelf THz imaging solutions or 2D-EO imaging techniques to avoid saturation or higher order effects. We further demonstrated complete assignment of the three differentially modulated signal channels and the light-matter interactions involved, which enabled characterization of the individual THz beam profiles simultaneously. Direct characterization of the nonlinear beam profile enables rigorous spatial and temporal optimization of the THz pump beams to maximize the signal strength of 2D THz spectroscopy, as evident by the precise spatial overlap achieved in this work with two independent THz emitters. This sensitive THz imaging method may open up new opportunities in non-colinear 2D THz spectroscopy to study fast vibrational dynamics within the first few ps, which are difficult to access in more common single-emitter setups.

References

[1] Harold Y. Hwang et al. “A review of non-linear terahertz spectroscopy with ultrashort tabletop-laser pulses”. *Journal of Modern Optics* 62.18 (2015), pp. 1447–1479.

[2] Peter Hamm et al. “Perspective: THz-driven nuclear dynamics from solids to molecules”. *Structural Dynamics* 4.6 (2017).

[3] Thomas Elsaesser, Klaus Reimann, and Michael Woerner. “Focus: Phase-resolved nonlinear terahertz spectroscopy - From charge dynamics in solids to molecular excitations in liquids”. *Journal of Chemical Physics* 142.21 (2015).

[4] Janne Savolainen, S. Ahmed, and Peter Hamm. “Two-dimensional Raman-terahertz spectroscopy of water”. *Proceedings of the National Academy of Sciences* 110.51 (2013), pp. 20402–20407.

[5] Klaus Reimann, Michael Woerner, and Thomas Elsaesser. “Two-dimensional terahertz spectroscopy of condensed-phase molecular systems”. *The Journal of Chemical Physics* 154.12 (2021), p. 120901.

[6] Frank Y. Gao et al. “High-speed two-dimensional terahertz spectroscopy with echelon-based shot-to-shot balanced detection”. *Optics Letters* 47.14 (2022), p. 3479.

[7] Haw-Wei Lin, Griffin Mead, and Geoffrey A. Blake. “ Mapping LiNbO 3 Phonon-Polariton Nonlinearities with 2D THz-THz-Raman Spectroscopy ”. *Physical Review Letters* 129.20 (2022), p. 207401.

[8] Jian Lu et al. “Coherent Two-Dimensional Terahertz Magnetic Resonance Spectroscopy of Collective Spin Waves”. *Physical Review Letters* 118.20 (2017), pp. 1–6.

[9] Jian Lu et al. “Nonlinear two-dimensional terahertz photon echo and rotational spectroscopy in the gas phase”. *Proceedings of the National Academy of Sciences* 113.42 (2016), pp. 11800–11805.

[10] Griffin Mead et al. “Sum-Frequency Signals in 2D-Terahertz-Terahertz-Raman Spectroscopy”. *Journal of Physical Chemistry B* 124.40 (2020), pp. 8904–8908.

[11] Courtney L. Johnson, Brittany E. Knighton, and Jeremy A. Johnson. “Distinguishing Nonlinear Terahertz Excitation Pathways with Two-Dimensional Spectroscopy”. *Physical Review Letters* 122.7 (2019), p. 73901.

[12] Q. Wu and X. C. Zhang. “Free-space electro-optic sampling of terahertz beams”. *Applied Physics Letters* 67.September 1995 (1995), p. 3523.

[13] A. Leitenstorfer et al. “Detectors and sources for ultrabroadband electro-optic sampling: Experiment and theory”. *Applied Physics Letters* 74.11 (1999), pp. 1516–1518.

[14] Jianming Dai, Jingle Liu, and Xi Cheng Zhang. “Terahertz wave air photonics: Terahertz wave generation and detection with laser-induced gas plasma”. *IEEE Journal on Selected Topics in Quantum Electronics* 17.1 (2011), pp. 183–190.

[15] Hichem Guerboukha, Kathirvel Nallappan, and Maksim Skorobogatiy. “Toward real-time terahertz imaging”. *Advances in Optics and Photonics* 10.4 (2018), p. 843.

[16] A. Rogalski and F. Sizov. “Terahertz detectors and focal plane arrays”. *Opto-Electronics Review* 19.3 (2011), pp. 346–404.

[17] Mostafa Shalaby, Carlo Vicario, and Christoph P. Hauri. “High-performing nonlinear visualization of terahertz radiation on a silicon charge-coupled device”. *Nature Communications* 6 (2015), pp. 1–5.

[18] O. V. Chefonov et al. “Terahertz beam spot size measurements by a CCD camera”. *Optics Letters* 44.17 (2019), p. 4099.

[19] Q. Wu, T. D. Hewitt, and X.-C. Zhang. “Two-dimensional electro-optic imaging of THz beams”. *Applied Physics Letters* 69.8 (1996), pp. 1026–1028.

[20] B. Monoszlai et al. “High-energy terahertz pulses from organic crystals: DAST and DSTMS pumped at Ti:sapphire wavelength”. *Optics Letters* 38.23 (2013), p. 5106.

[21] Robert W. Boyd. *Nonlinear Optics*. Vol. 53. Elsevier, 2003, pp. 1–578.

[22] Carlo Vicario, Mostafa Shalaby, and Christoph P. Hauri. “Subcycle Extreme Nonlinearities in GaP Induced by an Ultrastrong Terahertz Field”. *Physical Review Letters* 118.8 (2017), p. 083901.

[This chapter is temporarily embargoed.]

[This chapter is temporarily embargoed.]

Chapter 5

CONCLUSIONS AND FUTURE DIRECTIONS

5.1 Summary

This dissertation has advanced the capabilities of nonlinear terahertz spectroscopy by developing novel spatial characterization techniques and applying intense terahertz fields to disentangle complex dynamics in quantum materials. Through a combination of methodological innovation and fundamental material investigation, this work provides robust experimental frameworks for the optical manipulation of electronic and structural phases.

The first major contribution of this work established a sensitive imaging method for two-dimensional terahertz spectroscopy. By utilizing a differential chopping technique, we successfully isolated and characterized the nonlinear beam profile arising from the $\chi^{(3)}$ interaction. Implementing this method in two-dimensional Terahertz-Terahertz-Raman spectroscopy allowed us to retain identical pump beam paths and modify only the probe beam path. This approach eliminated the spatial and frequency distortions typically caused by the attenuators required in conventional imaging solutions to avoid saturation. By enabling the direct, simultaneous characterization of individual terahertz beam profiles, this methodology permits rigorous spatial and temporal optimization.

Building upon our control of intense terahertz fields, the second study successfully disentangled the structural and electronic degrees of freedom in the candidate excitonic insulator Ta_2NiSe_5. We exploited the spatial anisotropy of interband tunneling and introduced a geometric gating technique that selectively suppresses non-perturbative Keldysh carrier generation. By intentionally misaligning the driving field from the primary interband tunneling trajectory, we circumvented the causality dilemma that has hindered previous above-bandgap optical pumping experiments. Our approach successfully isolated the direct coherent structural response and selectively perturbed the lattice while leaving the excitonic condensate intact. This symmetry-selective gating establishes a highly efficient strategy to eliminate unwanted tunneling backgrounds in anisotropic, narrow-gap materials.

The final investigation explored the ultrafast nonlinear optical response of (110)-cut cubic zinc sulfide to propose a mechanism for dynamic terahertz polarization

control. Through multidimensional spectroscopy, tunable narrowband pumping, and quantitative field-scaling analyses, we systematically eliminated indirect excitation pathways such as anharmonic coupling, different frequency generation, and pulse mixing. We definitively assigned the observed one-dimensional spectral oscillations to a macroscopic phase mismatch between the co-propagating terahertz pump and the optical probe. Exploiting this temporal walk-off enabled the extraction of a highly anisotropic transient refractive index. We demonstrated that the terahertz-induced birefringence closely satisfies the theoretical requirements for a broadband quarter-waveplate. Relying on an instantaneous nonlinear response rather than physical thickness, this work successfully proposes a prototype platform for generating circularly polarized terahertz pulses to dynamically break time-reversal symmetry in topological materials.

5.2 Future Directions

The methodologies and findings presented in this dissertation pave the way for several compelling avenues of future research.

The two-dimensional terahertz focusing method and the powerful differential imaging technique provide rich spatial and temporal information regarding the nonlinear focal volume. Future optical engineering efforts can leverage this multidimensional data to map the chromatic distribution in space of a terahertz focus. Understanding how different frequency components are spatially distributed at the focus will be highly beneficial for optimizing broadband terahertz nonlinear experiments and correcting subtle spatiotemporal aberrations in complex optical setups. Furthermore, because this sensitive imaging technique successfully achieves precise spatial overlap with two independent emitters, it directly opens new opportunities for non-colinear multidimensional terahertz spectroscopy to probe fast vibrational dynamics in the picosecond regime.

For the study of Ta_2NiSe_5, our geometric gating technique proved that selectively suppressing the Franz-Keldysh tunneling cross section provides a robust pathway to preserve the excitonic ground state. Because this method successfully isolates the macroscopic phase transition, future investigations should employ transient absorption spectroscopy aligned along various crystallographic axes. This will provide novel information regarding the anisotropic conductivity properties of the condensate. Furthermore, utilizing terahertz pump and time-resolved angle-resolved photoemission spectroscopy probe techniques, as well as terahertz pump and

terahertz probe spectroscopy, should yield new insights. For example, such advanced probe techniques can explicitly map how intense terahertz fields geometrically control the generation of Franz-Keldysh tunneling across the Brillouin zone.

Finally, the dynamic birefringence observed in oriented zinc sulfide offers an exciting blueprint for ultrafast optical engineering. While our angle-dependent experiments extracted an extraordinary refractive index in a cubic crystal driven by an intense pump, we have currently only proposed this system as a theoretical prototype for a waveplate. Future experimental efforts must focus on physically engineering and demonstrating a fully functional broadband terahertz quarter-waveplate based on this transient birefringence. Successfully realizing this proposed device will unlock new frontiers in Floquet engineering, allowing researchers to drive foundational low-energy excitations and achieve the on-demand optical manipulation of topological quantum states.

Appendix A

ECHELON-BASED SINGLE-SHOT DETECTION

In this chapter, I will explain the procedure for processing echelon-based single-shot THz detection. The fundamental alignment principle involves creating a clear echelon image on a camera through the off-axis parabolic mirror hole. The horizontal axis of the resulting image carries temporal information, whereas the vertical axis does not contain spectral information. To maximize the photon count, the signal can be summed vertically, either through data processing or by applying vertical focusing techniques. Once a clear camera image is established, the time delay can be extracted using the camera software.

The following sections detail the operation of the camera via the MATLAB graphical user interface (GUI). Throughout this chapter, the Thorlabs Kiralux 2.3 MP Monochrome CMOS Camera (CS235MU) is used as the primary example. However, by updating the communication protocols and the camera control and data extraction APIs, the subsequent post-processing code can be adapted for various camera systems. The detailed software flowchart is shown in **Fig. A.1**.

A.1 Operation

The data processing software was co-developed by Dr. Haw-Wei Lin and the author. As shown in **Fig. A.2**, the main page of the user interface allows the user to acquire data and adjust common experimental parameters. When launching the `.mlapp` file, the software provides an option to browse existing data files without initiating the camera connection sequence. This prevents connection errors when the USB is unplugged. The "Browse File" button allows the user to open and compare time-domain data, including newly acquired measurements. Checking the "Coadd" box displays the summed result of an experimental file. If left unchecked, the software plots the individual time traces for each run within the selected file.

To begin an experiment, ensure the camera is connected to the computer via a USB 3.0 interface and that the external trigger source is connected to the camera. This software is configured exclusively for external hardware triggering. For other trigger modes, please refer to the camera's control manual.

Click the "Connect" button to establish communication. Upon a successful

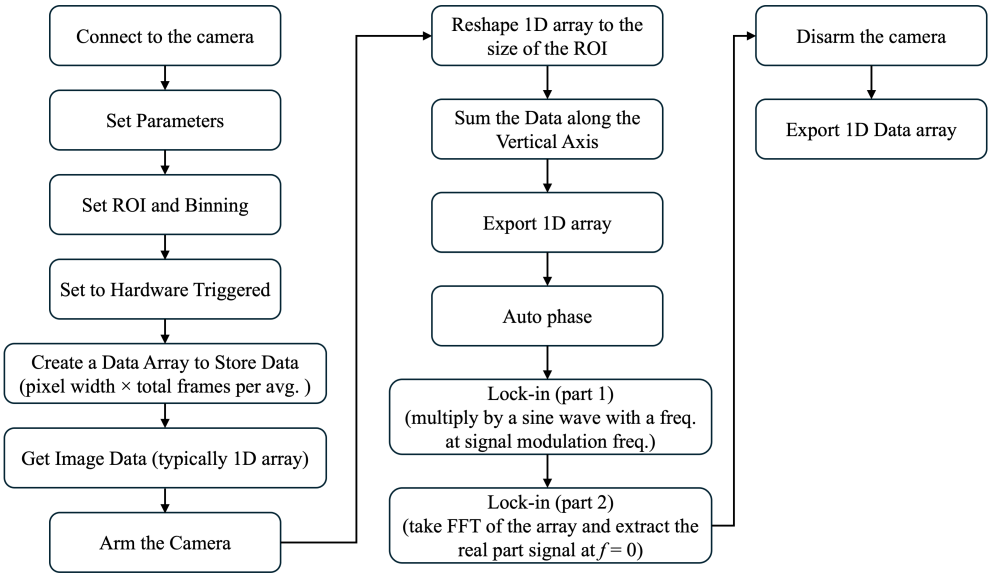

Figure A.1: Flowchart of the camera control and data processing software. The diagram outlines the sequence of operations within the MATLAB architecture, detailing the logical progression from the initial connection and parameter configuration to image acquisition, data summation, and auto phase.

connection, the connection indicator will turn green, the status indicator will turn green and display “Idle”, and the camera’s physical LED will turn blue. Note that a green LED indicates only a USB 2.0 connection is established.

Several parameters must be configured. The **Exposure Time** is the duration of data collection per individual trigger event. The **Integration Time** is the total accumulated exposure time before the data is written to a single file. Finally, the **Number of Averages** defines the number of times a single integration cycle is repeated.

Care must be taken when setting these values. If the integration time is too long, the computer or camera memory buffer may overflow, potentially crashing the program and resulting in lost data. The author recommends keeping the integration time under 120 seconds. Conversely, if the integration time is too short, the signal-to-noise ratio (S/N) may be insufficient for the “Auto Phase” function to accurately determine if the signal phase is positive or negative. This failure can cause successive averages to cancel each other out. An integration time between 10 and 120 seconds is generally optimal.

To maximize signal quality, the camera’s well depth should be filled as much as possible. For oscillator systems, increasing the exposure time allows more photons

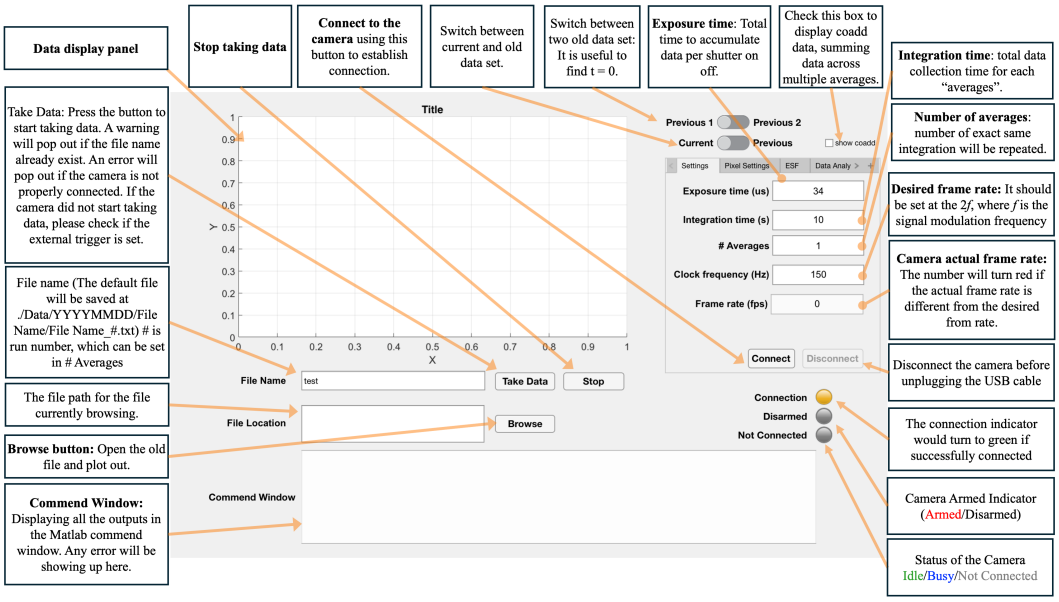

Figure A.2: Primary user interface of the data acquisition software. The main page enables users to establish hardware connections, configure experimental timing parameters, and execute data collection. The central plot allows for visualization of the THz signal, supported by data processing tools for signal coadd and plot overlay on the right.

to be collected per exposure, directly improving the S/N ratio. For amplifier systems operating at a 1 kHz repetition rate, there is only one laser shot per exposure. In this case, as long as the laser pulse falls within the exposure window, increasing the exposure time does not accumulate more signal. Instead, the exposure time should be minimized to reduce the collection of ambient background photons, thereby improving the S/N ratio.

To adjust the exposure time, the camera must be actively connected. The GUI will update to reflect the new setting once it is successfully applied. If the displayed exposure time differs slightly from the requested value, it is because the camera hardware only accepts increments of 20 μs, with a minimum possible exposure time of 34 μs.

A long exposure time inherently limits the maximum achievable frame rate. If a frame rate warning appears after adjusting the exposure time, the user must select a lower frame rate or shorten the exposure. The author has observed that running the camera at a high frame rate combined with a very short exposure time can decrease the overall duty cycle for photon collection.

To stop data acquisition, press the "Stop" button. Before physically unplugging the

USB cable, the communication must be properly terminated by either clicking the "Disconnect" button or closing the software entirely.

A.2 Advanced Camera Controls

Advanced camera functions can be accessed via the designated tabs, as illustrated in **Fig. A.3**. To adjust the Region of Interest (ROI), which defines the active pixel area for data readout, the camera must be connected. After defining the ROI, press "Apply" to update the camera settings. The Edge Spread Function (ESF) feature is detailed in the subsequent section.

The "Data Analysis" tab provides useful statistical metrics for evaluating experimental conditions and optimizing the signal peak. Finally, the "Auto Phase" function is critical when multiple modulation frequencies are used to isolate the THz-THz-Raman (TTR) signal. Because the modulation cycle consists of six stages, as shown in **Fig. 2.3**, different stages require specific phase locking. However, in 1D experiments, the camera only records "pump-on" and "pump-off" states. The software corrects this by multiplying the trace by -1 if the peak amplitude is inverted, ensuring that different averages maintain phase alignment.

A.3 Estimating Cutoff Frequency from an Edge Response

The spatial resolution limit can be estimated by analyzing the system's response to a sharp spatial edge, known as the knife-edge test. This method maps the empirical spatial spread of an edge into the frequency domain to determine the maximum resolvable bandwidth. The raw intensity data measured across the edge could include spikes. To obtain a clean representation of the boundary, the data is fitted to a continuous function, specifically a Fermi-Dirac distribution. This mathematical model defines the Edge Spread Function (ESF):

$$ESF(x) = a + \frac{b}{1 + \exp\left(\frac{x-c}{d}\right)} \tag{A.1}$$

where x is the spatial coordinate (e.g., pixel position), a and b define the baseline and amplitude of the intensity step, c represents the central spatial coordinate of the edge, and d represents the "blur" of the transition.

The system's one-dimensional spatial impulse response is given by the Line Spread Function (LSF). Mathematically, the LSF is the first spatial derivative of the ESF. By differentiating the fitted logistic curve, the step transition is transformed into a localized peak:

Figure A.3: Advanced settings and data analysis interface. The advanced configuration panel allows users to customize camera hardware settings and evaluate signal. The "Pixel Settings" tab provides controls for defining the Region of Interest (ROI) and binning. The "Data Analysis" tab displays statistical metrics useful for optimizing experimental conditions and maximizing the signal peak. Additional tabs include the Edge Spread Function (ESF) processing tool and the "Auto Phase" function, which automatically corrects for phase inversions when isolating the signal phase negative.

$$LSF(x) = \frac{d}{dx} ESF(x) \tag{A.2}$$

The full-width at half-maximum (FWHM) of this LSF peak provides a direct time-domain measure of the spatial resolution.

To evaluate the resolution limit in the spatial frequency domain, the Modulation Transfer Function (MTF) is calculated. The absolute MTF is defined as the magnitude of the Fourier Transform of the LSF. Let ν_x represent the spatial

frequency. The MTF is given by

$$MTF(\nu_x) = \left| \int_{-\infty}^{\infty} LSF(x) e^{-i2\pi\nu_x x} dx \right| \tag{A.3}$$

In practice, this is computed using a discrete Fast Fourier Transform (FFT). To evaluate image contrast on a standardized scale, the MTF is normalized against its zero-frequency (DC) component, establishing a relative contrast scale from 0 to 1:

$$MTF_{norm}(\nu_x) = \frac{MTF(\nu_x)}{MTF(0)} \tag{A.4}$$

The absolute resolution limit of the system is defined by a specific contrast threshold. In standard practice, the spatial cutoff frequency (ν_c) is determined as the point where the normalized MTF contrast drops to 5%. This is evaluated by finding the root of the condition:

$$MTF_{norm}(\nu_c) = 0.05 \tag{A.5}$$

For time-domain spectroscopy systems, the spatial frequency limit (ν_c, in cycles/mm) must be mapped to a temporal bandwidth limit (ν_{THz}, in THz). This mapping depends on the specific hardware architecture used to encode optical delay.

For a system utilizing a reflective echelon mirror, time is mapped statically across the spatial axis of the sensor. The spatial-to-temporal conversion relies on an effective calibration velocity (v_{eff}), defined by the temporal delay per pixel (Δt_{pixel}) and the physical pixel pitch (Δx_{pixel}):

$$v_{eff} = \frac{\Delta x_{pixel}}{\Delta t_{pixel}} \tag{A.6}$$

The temporal cutoff frequency is then calculated via direct linear scaling:

$$\nu_{THz} = \nu_c \cdot v_{eff} \tag{A.7}$$